

Ab-initio study of the effect of bromide mixing into RbPbI₃ on the structural, electronic and optical properties

Anupriya Nyayban* and Subhasis Panda†

Department of Physics

National Institute of Technology Silchar, Assam, 788010, India

Avijit Chowdhury‡

Department of Physics

National Institute of Technology Silchar, Assam, 788010, India
and

Department of Condensed Matter Physics and Material Sciences,
S.N. Bose National Centre for Basic Sciences, JD Block,
Sector III, Salt Lake City, Kolkata 700106, India

(Dated: April 4, 2022)

The ultra-high efficiency and cost-effective photovoltaics based on halide perovskites have brought a revolution to ongoing photovoltaic research, surpassing the expectations of the scientific community. However, structural stability is a severe issue that hinders their wide-scale integration at the device level. Compositional engineering with the halide mixing has become an efficient way to deal with this issue without compromising device efficiency. Herein, the structural, electronic and optical properties of the bromide mixed orthorhombic RbPb(I_{1-x}Br_x)₃ (where, $x = 0.25, 0.50$ and 0.75) are calculated using the density functional theory. The electronic bandstructure and density of states (DOS) are calculated using both PBE (Perdew-Burke-Ernzerhof) and TB-mBJ (Tran Blaha modified Becke Johnson) potential. The lowest energy bandgaps of 2.288 and 2.986 eV for bromide mixing of $x = 0.50$ are obtained using PBE and TB-mBJ, respectively. In contrast, the mixed bromide phases possess a smaller effective mass, facilitating a better carrier transport through the mixed halide. Using PBE, the excitons appear to be the Mott-Wannier type. However, the TB-mBJ predicts the exciton to be Frenkel type for bromide mixing of $x = 0.75$ and a Mott-Wannier type for all other mixing under study. The spectroscopic limited maximum efficiency (SLME) is observed to be at the highest values of 14.0% and 4.1% for the equal admixture of I and Br using PBE and TB-mBJ, respectively. The calculated properties are consistent with the reported data of the similar structures.

I. INTRODUCTION

Hybrid halide perovskites have been the most studied material recently in the photovoltaic group due to its superior properties for solar cell applications such as suitable bandgap and band alignment [1–4], strong absorption [5, 6], better charge transport [7–11] and lower defect properties [12–14]. Moreover, halide perovskites are processed by solution methods with the lower cost and compositional materials are abundant in nature [15, 16]. In spite of these excellent properties, the instability of organic-inorganic halide perovskites due to heat, oxygen, moisture and light [17–20] prevent them to be commercialized. Normally, inorganic materials exhibit better stability in terms of temperature than the organic one [21–24]. The unencapsulated MAPbBr₃ based device exhibit a faster 55% decay of the phototcurrent density compared to the maximum value during an illumination of 5 h whereas CsPbBr₃ based one shows only 13% decay [25]. Additionally, MAPbBr₃ based cell faces 85% efficiency loss in an environment of 60 – 70 % relative humidity for 2 weeks whereas CsPbBr₃ based cell shows almost no loss [25]. However, all inorganic perovskites were not popular due to their lower efficiency. Recently, the Cs-based perovskite is reported [26] in 2016 to achieve the efficiency of 10% by tuning the bandgap with adjusting ratio of iodide-bromide. The mixed halide perovskite based solar cells which is deposited using all-vacuum-deposition technique, also shows the surplus efficiency of 11% [27]. In the similar time, CsPbI₃-based quantum dot solar cell not only exhibits efficiency of 11% but also it poses the phase stability [28]. Thereafter, these research efforts have inspired researchers to have an in-depth insight into the fundamental properties of all inorganic perovskites for better functionality.

The halide mixing i.e. the mixing of multiple halogen elements are very popular in recent trend due to the several beneficial effects. Firstly, the halide mixing increases the stability e.g. MAPbI_{3-x}Cl_x are reported [29] to possess

* anupriya_rs@phy.nits.ac.in

† subhasis@phy.nits.ac.in

‡ avijitiacs@gmail.com

remarkable stability in air as compared to MAPbI₃. MAPbI₃ with 20 – 29% Br mixing is also found [30] to improve the stability tremendously without changing the efficiency. Secondly, mixed halide perovskites enhance the transport of charge carriers. The longer charge carrier diffusion length is observed [31–33] in MAPbI_{3-x}Cl_x than MAPbI₃. The improved mobility and the reduced recombination rates are also reported [34, 35] in both MAPbI_{3-x}Br_x and MAPbBr_{3-x}Cl_x. Third, bandgap can be tuned by halide mixing in halide perovskites. Chloride mixed MAPbBr₃ i.e. MAPbBr_{3-x}Cl_x are observed [35] to exhibit better photovoltaic performance having the higher open circuit voltage of 1.5 eV and the reduced short circuit current. MAPbI_{3-x}Br_x are also observed [36] to be suitable for the colorful solar cell design in order to found the energy saving buildings. These reported findings suggest that the halide mixing into the inorganic halide perovskites could be an efficient way to improve the photovoltaic performances. Moreover, no literature is found for the iodide-bromide mixed RbPbI₃ i.e. RbPb(I_{1-x}Br_x)₃ towards the electronic and optical properties.

In this work, we have systematically studied the effect of the bromide mixing into RbPbI₃ (with Br concentration of 0.25, 0.50 and 0.75) on the structural, electronic and optical properties. The work is arranged in the following manner: Section II describes the computational methods; Section III-A provides the structural information; Section III-B describes the electronic structures in detail including the density of states (DOS) and the bandstructures; Section III-C informs extensively regarding the optical properties, effective masses of the photo-generated charge carriers, the spectroscopic limited maximum efficiency (SLME); and at last the work is summarized and concluded in the section IV.

II. COMPUTATIONAL DETAILS

At first, $2 \times 2 \times 2$ supercell is constructed for RbPb(I_{1-x}Br_x)₃ (when $x = 0.25, 0.50$ and 0.75) from an optimized orthorhombic RbPbI₃ of *Pnma* space group [37]. Then the supercell is relaxed and optimized. All the density functional theory (DFT) based calculations have been performed using WIEN2k [38]. A muffin tin radius of 2.50 Å is set for all the atoms whereas a Rk_{\max} of 7 is set for all the structures. Perdew-Burke-Ernzerhof (PBE) [39] exchange correlation functional has been reported [40–43] to estimate the bandgap accurately for the halide perovskites without considering the spin orbit coupling (SOC) effect. Again PBE including SOC are reported [44] to underestimate the bandgap but does not alter the pattern of the bandstructure. Additionally the hybrid functional is also reported [45] to overestimate the bandgap whereas less computationally demanding TB-mBJ (Tran Blaha modified Becke Johnson) [46] potential is found to estimate the bandgap more accurately [47, 48]. Therefore, PBE and TB-mBJ potentials are used to find both the electronic and optical properties for all I-Br mixed structures. The electronic properties are estimated with a k mesh of $1 \times 5 \times 11$ for $x = 0.50$ and $2 \times 3 \times 14$ for both $x = 0.25$ and 0.75 , respectively. For the calculation of optical properties, a denser k mesh of $3 \times 11 \times 25$ for $x = 0.50$ and $4 \times 7 \times 31$ for other two structures, respectively.

III. RESULTS AND OBSERVATIONS

A. Optimized Structures

RbPbI₃ have orthorhombic NH₄CdCl₃ type structure of *Pnma* space group at room temperature. A supercell of $2 \times 2 \times 2$ has been considered from the optimized pristine RbPbI₃ unit cell [37]. The iodide has been gradually replaced with bromide by the concentration x of Br. PBE-GGA have been used to find the structural properties. The total energy with the variation of the supercell-volume are fitted using Birch-Murnaghan equation of state [49] as shown in FIG. S1 in the supporting information. The optimized supercells are also depicted in FIG. S2 in the supporting information. The estimated lattice parameters, volume of supercell (V_0), bulk modulus (B) and pressure derivative (B') for RbPb(I_{1-x}Br_x)₃ are listed in TABLE I. The lattice parameters decrease with the increasing Br-concentrations except for $x = 0.50$. The decrease in lattice parameters is attributed to the reduced Br radii.

TABLE I: Lattice parameters for RbPb(I_{1-x}Br_x)₃ systems

x	a (Å)	b (Å)	c (Å)	V_0 (Å ³)	B (GPa)	B' (GPa)
0.25	34.060	20.149	4.681	3212.151	12.8517	7.5097
0.50	34.533	10.214	4.746	1673.957	11.8370	10.1306
0.75	33.789	19.989	4.643	3136.202	11.7332	7.2820

B. Electronic Properties

The electronic properties are investigated with both PBE and TB-mBJ potentials. The electronic band structures along the high symmetry k -point $\Gamma \rightarrow X \rightarrow S \rightarrow Y \rightarrow \Gamma \rightarrow Z \rightarrow U \rightarrow R \rightarrow T \rightarrow Z$ are shown in FIG. 1. The band gap estimated with PBE is ranging from 2.288 to 2.435 eV while that with TB-mBJ potentials is from 2.986 to 3.253 eV for the increasing Br-content. The valence band maximum (VBM) is observed at a k point between $\Gamma \rightarrow Z$ path for all the halide mixed systems under consideration. Again, the conduction band minimum (CBM) is found at Γ and S for ($x = 0.25$ & 0.75) and ($x = 0.50$), respectively, confirming all I-Br mixed structures to have indirect band gap. All the calculated band gap values are listed in TABLE II. The band gap decreases with the increase of the percentage of Br due to the reduced lattice parameters. The lowest band gap is observed for the equal mixture of I and Br. The band gap estimated with TB-mBJ potential agrees well with the experimental values for the halide mixed CsPbI₃ systems [50]. TB-mBJ potential uplifts the CBM towards the higher energy and thus, widens the band gap values. No significant changes in the valence band as well as in the nature of the bandstructure is observed. The band gap of the RbPb(I_{1-x}Br_x)₃ is reduced compared to that of both pristine RbPbI₃ and RbPbBr₃ [37]. The similar behavior of the bandstructures calculated with both PBE and TB-mBJ is also observed for RbPbI₃ [37].

TABLE II: The band gap E_g in eV for all RbPb(I_{1-x}Br_x)₃ mixed systems

	x=0.25	x=0.50	x=0.75
PBE	2.366	2.288	2.435
TB-mBJ	3.025	2.986	3.253

The atomic orbital contribution has been explored using the density of state (DOS) estimation in order to investigate the electronic structure in brief. Partial density of states (PDOS) calculated with PBE and bandstructures calculated using PBE and TB-mBJ for all the mixed halide systems are shown in FIG. 1. Rb has no contribution in either VBM or CBM and hence, the orbital contributions of Pb, I and Br are only shown. The first CB is mainly dominated with 6p orbital of Pb. The range of the first CB are from 2.48 to 4.47, 2.52 to 4.61 and 2.53 to 5.10 eV corresponding to the increasing Br-content of 0.25, 0.50 and 0.75, respectively. The first valence band (VB) is dominantly contributed by both Br-4p and I-5p with a small contribution of Pb-6p towards the lower energy region of the first VB. Pb-6s contributes to the second VB. The first VB expands from 0.00 to -2.82, -3.06 and -3.21 eV for $x = 0.25, 0.50$ and 0.75 , respectively. I-5p and Br-4p contributes more to the uppermost and lowermost region of the first VB, respectively.

The total density of states (TDOS) for all RbPb(I_{1-x}Br_x)₃ systems are shown in FIG. 1d. The increase in TDOS is higher for both $x = 0.25$ and 0.75 than that for $x = 0.50$. The VB rises higher than the CB. The higher and lower concentration of Br exhibit the higher probability of larger carrier concentrations due to the larger TDOS and therefore, can increase the transport properties too. The similar phenomena are also observed for MAPb_{1-x}Ge_xI₃ [51].

C. Optical Properties

The optical properties for all I-Br mixed RbPb(I_{1-x}Br_x)₃ systems are investigated with both PBE and TB-mBJ potential. All the optical properties are estimated using the complex dielectric function ($\epsilon(\omega) = \epsilon_1(\omega) + i\epsilon_2(\omega)$). At first, the momentum matrix using the occupied and unoccupied states are used to calculate the imaginary part of the dielectric function ($\epsilon_2(\omega)$). The variation of $\epsilon_2(\omega)$ with the photon energy are calculated using both PBE and TB-mBJ potential as show in FIG. 2a and FIG. 2c, respectively. The strongest peaks of $\epsilon_2(\omega)$ calculated with PBE are observed at 4.503, 4.204, 3.714; 5.102, 4.667, 4.912; 4.776, 4.531, 3.878 eV for bromide concentrations of 0.25, 0.50 and 0.75 along xx, yy and zz polarization directions, respectively. The spectrum of $\epsilon_2(\omega)$ calculated with TB-mBJ potential has the strongest peaks at the photon energy of 5.048, 4.966, 4.503; 5.755, 5.129, 5.429; 5.455, 5.510, 4.639 eV along three different directions for the increasing Br concentrations of 0.25, 0.50 and 0.75, respectively. The trend of observed peaks in $\epsilon_2(\omega)$ are the result of the increasing bandgap with the increasing Br percentage (except at $x = 0.50$).

The real part of the dielectric function ($\epsilon_1(\omega)$) is calculated using Kramer-Kronig relation, once $\epsilon_2(\omega)$ has been estimated. Then extinction coefficient ($k(\omega)$), refractive index ($n(\omega)$), absorption coefficient ($\alpha(\omega)$) and reflectivity ($R(\omega)$) are calculated using the real ($\epsilon_1(\omega)$) and imaginary part ($\epsilon_2(\omega)$) of the dielectric function [26].

The spectrum of the absorption coefficient calculated using PBE and TB-mBJ are shown in FIG. 2b and FIG. 2d, respectively. The strongest peaks of the absorption spectrum calculated with PBE correspond to the photon energy of 5.157, 4.667, 4.558; 5.401, 4.966, 4.803; 5.320, 5.891, 5.157 eV along xx, yy and zz directions for $x = 0.25, 0.50$ and 0.75 , respectively. In case of the absorption spectrum calculated with TB-mBJ potential, the strongest peaks

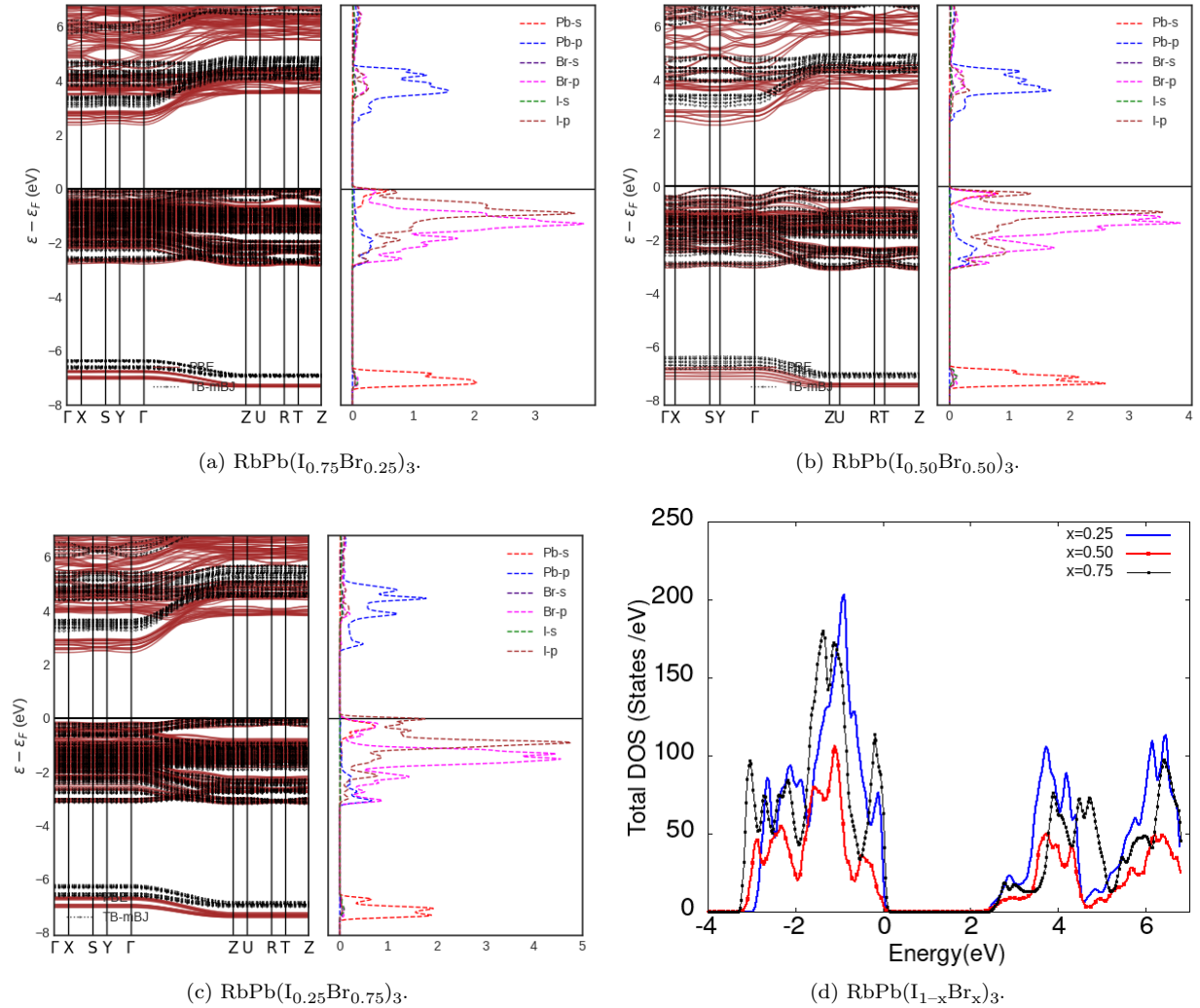


FIG. 1: The band structures along with the partial density of states (PDOS) and total density of states (TDOS) for all the bromide mixed systems.

along three different directions are observed at 5.782, 5.674, 5.429; 6.055, 5.782, 5.674; 6.517, 6.517, 6.435 eV for the increasing Br percentage of 0.25, 0.50 and 0.75, respectively. The transition of electrons from I-5p, Br-4p and Pb-6s mixed valence state to the conduction state consisting of Pb-6p is mainly dominant for the strongest peaks of the absorption spectrum in all $\text{RbPb}(\text{I}_{1-x}\text{Br}_x)_3$ systems. The blueshift towards the higher energy region is observed for all I-Br mixed systems with the increasing Br percentage and this shift is attributed to the increasing bandgap. The absorption spectra shows that iodide-bromide mixed $\text{RbPb}(\text{I}_{1-x}\text{Br}_x)_3$ systems can absorb photons from wider energy region (visible and ultraviolet) as compared to the pristine RbPbI_3 case. The nature of the absorption spectrum calculated with both PBE and TB-mBJ are similar whereas the blueshift toward the higher energy for TB-mBJ potential is more than that for PBE. Furthermore, the integration over the absorption coefficient along near-infrared (0 – 1.7 eV), visible (1.7 – 3.3 eV) and ultraviolet (3.3 – 5.0 eV) regions of the solar spectrum are calculated for all the considered systems and listed in TABLE IV. The average integrated intensity decreases with the increasing concentrations of Br. The average absorption intensity decreases more with the bromide mixing in RbPbI_3 than that for the pristine RbPbI_3 .

The real part of the dielectric function ($\epsilon_1(\omega)$), reflectivity ($R(\omega)$) and refractive index ($n(\omega)$) spectrum are shown in FIG. S3 of the supporting information and their static values are listed in the TABLE III. The average static dielectric constant ($\epsilon_1(0)$) calculated with PBE and TB-mBJ are 4.802, 4.476, 4.066; 3.887, 3.610 and 3.239 with the increasing Br percentage of 0.25, 0.50 and 0.75, respectively. The static dielectric constant $\epsilon_1(0)$ calculated with PBE of I-Br mixed RbPbI_3 systems are larger than that of pristine RbPbBr_3 but are smaller than that of pristine RbPbI_3

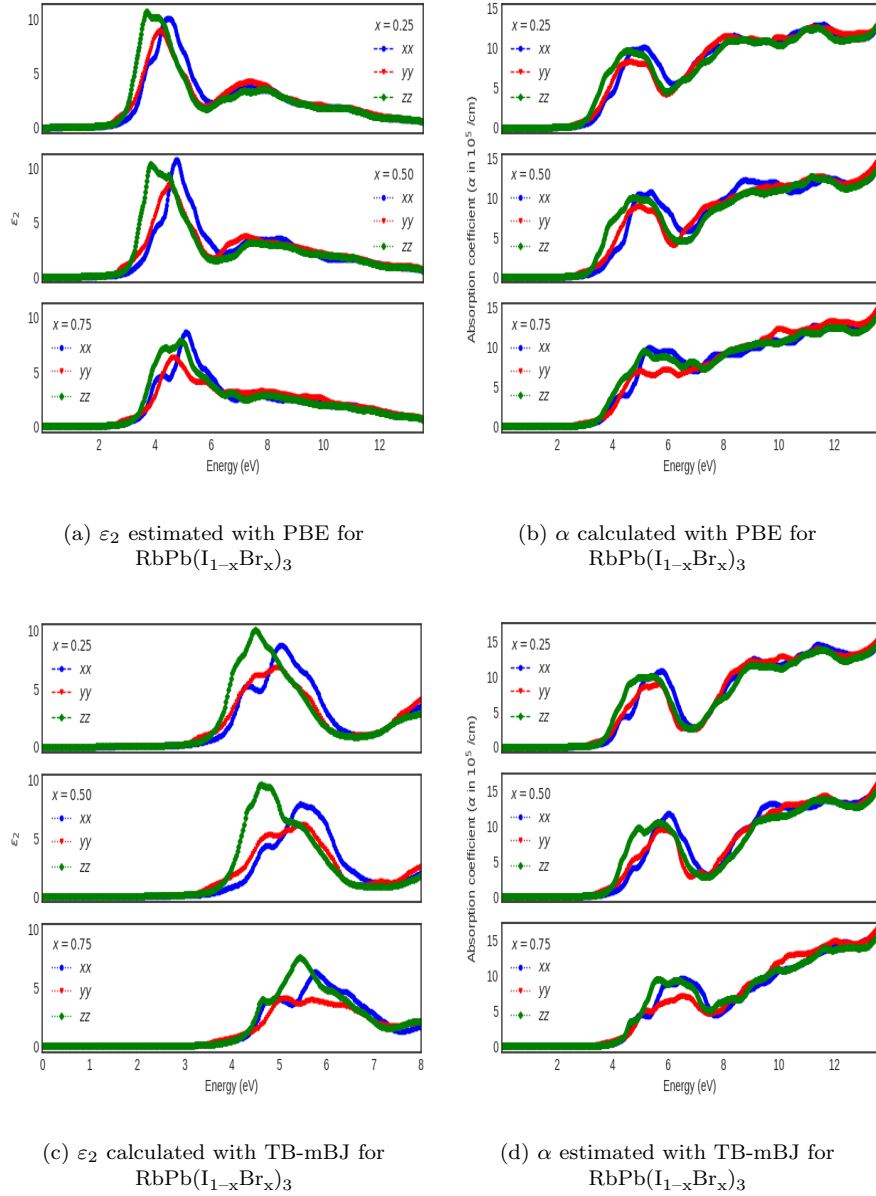


FIG. 2: The variation of the imaginary part of the dielectric function (ε_2) and the absorption coefficient (α) with the photon energy along three different polarization direction for $x = 0.25, 0.50$ and 0.75 , respectively.

TABLE III: The static dielectric constant, reflectivity, refractive index, binding energy of excitons and the radius of the lowest bound states for all the systems.

x		$\varepsilon_1(0)$			$R(0)$			$n(0)$		
		(100)	(010)	(001)	(100)	(010)	(010)	(100)	(010)	(010)
0.25	PBE	4.673	4.625	5.107	0.135	0.133	0.149	2.162	2.151	2.260
	TB-mBJ	3.818	3.757	4.085	0.104	0.102	0.114	1.954	1.938	2.021
0.50	PBE	4.302	4.313	4.814	0.122	0.122	0.140	2.074	2.077	2.194
	TB-mBJ	3.492	3.485	3.852	0.092	0.091	0.106	1.869	1.867	1.963
0.75	PBE	4.045	3.868	4.286	0.113	0.106	0.122	2.011	1.967	2.070
	TB-mBJ	3.252	3.093	3.371	0.082	0.076	0.087	1.803	1.759	1.836

[37]. A large static dielectric constant value will help to reduce the recombination of electron and hole and, thus, will

increase the device performance. The average static refractive index ($n(0)$) calculated with PBE and TB-mBJ are 2.191, 2.115, 2.016; 1.971, 1.900 and 1.799 for $x = 0.25, 0.50$ and 0.75 , respectively. The refractive index decreases with the increasing bromide percentage for the considered halide mixed RbPbI₃ systems. The average static reflectivity ($R(0)$) using both PBE and TB-mBJ are estimated as 13.9%, 12.8%, 11.4%; 10.7%, 9.6% and 8.2% for the increasing Br content of 0.25, 0.50 and 0.75, respectively. The reflectivity decreases with the increasing Br content which agrees with the fact of the higher reflectivity for RbPbI₃ than that of RbPbBr₃ [37].

TABLE IV: The calculated average integrated absorption intensity in 10^3 eV/cm for RbPb(I_{1-x}Br_x)₃

Energy range (eV)	PBE			TB-mBJ		
	0 – 1.7	1.7 – 3.3	3.3 – 5.0	0 – 1.7	1.7 – 3.3	3.3 – 5.0
x = 0.25	2.420	60.817	1107.416	1.562	14.873	649.619
x = 0.50	2.074	38.331	935.044	1.340	9.951	457.450
x = 0.75	1.687	24.472	630.978	1.051	6.525	224.397

TABLE V: Effective masses for RbPb(I_{1-x}Br_x)₃

Directions	x=0.25		x=0.50		x=0.75		E_b (meV)	a^* (Å)	
	Electron	Hole	Electron	Hole	Electron	Hole			
PBE	X → S	0.129	0.076	0.347	0.056	0.058	0.158	44.8	33.4
TB-mBJ		0.107	0.289	0.566	0.069	0.117	0.383	58.5	31.6
PBE	Y → Γ	0.085	0.177	0.346	0.074	0.118	0.127	29.8	53.8
TB-mBJ		0.110	0.292	0.566	0.083	0.118	0.335	56.3	35.3
PBE	Γ → Z	0.038	2.212	0.068	0.032	0.029	0.252	32.1	55.1
TB-mBJ		0.039	0.256	0.074	0.034	0.034	0.217	147.8	15.0

Moreover, the effective masses of the photo induced electrons and holes are also estimated using both PBE and TB-mBJ potential. The top of the VB and bottom of the CB are fitted to a parabola and then the effective masses are calculated from the following relation:

$$m_{eff} = \hbar^2 \frac{1}{\frac{\partial^2 E(k)}{\partial k^2}} \quad (1)$$

where, k and $E(k)$ are the wave vector and the energy corresponding to the top and bottom of the VB and CB, respectively. The calculated effective masses of electrons and holes along the high symmetry k path of $X \rightarrow S$, $Y \rightarrow \Gamma$ and $\Gamma \rightarrow Z$ are listed in TABLE V. The average effective masses of electrons (m_e) and holes (m_h) calculated using PBE are 0.084, 0.254, 0.068 and 0.822, 0.054, 0.090 for $x = 0.25, 0.50$ and 0.75 , respectively. The reduced effective masses are then estimated using: $\mu = \frac{m_e m_h}{m_e + m_h}$ and found to be 0.076, 0.044 and 0.039 for the increasing Br percentage as 0.25, 0.50 and 0.75, respectively. Using TB-mBJ potential the average effective masses of electrons and holes are 0.085, 0.402, 0.179 and 0.279, 0.062, 0.312 for $x = 0.25, 0.50$ and 0.75 in the mixed halide systems, respectively. The reduced effective masses resulted from TB-mBJ are 0.065, 0.54 and 0.114 corresponding to $x = 0.25, 0.50$ and 0.75 , respectively. The reduced effective mass calculated using PBE decreases with the increasing Br content whereas it increases when μ is calculated from TB-mBJ. The effective masses of I-Br mixed RbPbI₃ structures are found to be lesser than that of the pristine RbPbI₃ [37].

The effective masses and the static dielectric constants are important parameters to find the binding energy (E_b) of the excitons. The binding energy and the radius of the lowest bound state (a^*) are estimated using $E_b = \frac{13.6 \times \mu}{\epsilon_1(0)^2}$ and $a^* = \frac{\epsilon_1(0) \times a_0}{\mu}$ (where, $a_0 =$ Bohr radius), respectively. All the values of E_b and a^* for all I-Br mixed systems are listed in TABLE V. The binding energy of excitons calculated using PBE and TB-mBJ are 44.8, 29.8, 32.1 and 58.5, 56.3, 147.8 for the increasing Br percentage as 0.25, 0.50 and 0.75, respectively. The binding energy of excitons are smaller for all the systems except that for $x = 0.75$ when it is calculated using TB-mBJ potential. The calculated radius of the lowest bound state as listed in TABLE V are found to be larger than the lattice parameters for all cases except $x = 0.75$ using TB-mBJ potential. Therefore, the calculations using PBE suggest excitons for all cases to be Mott-Wannier type. The calculations using TB-mBJ predicts the excitons for both $x = 0.25$ and 0.50 are of Mott-Wannier type whereas it is of Frenkel type for $x = 0.75$. This is also agreed well with the fact that excitons using PBE are of Mott-Wannier type for both pristine RbPbI₃ and RbPbBr₃ [37].

Moreover, the spectroscopic limited maximum efficiency (SLME) are also calculated using both PBE exchange correlation functional and TB-mBJ potential for all the considered halide mixed systems and are shown in FIG. 3.

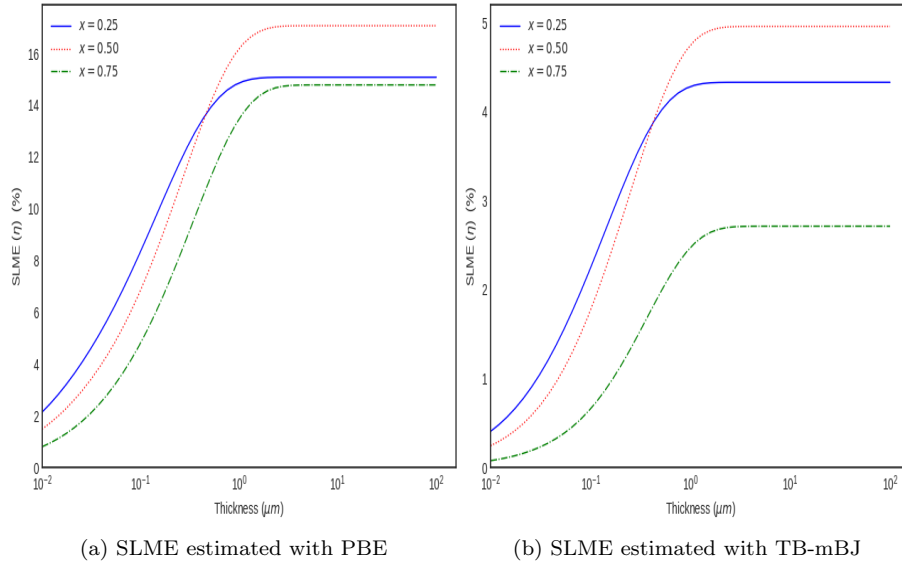


FIG. 3: SLME estimated with PBE and TB-mBJ for $\text{RbPb}(\text{I}_{1-x}\text{Br}_x)_3$.

The absorption coefficients and bandgaps calculated from the first principle calculations are used to estimate SLME. All the required formulae and input data calculated using the first principle calculations as shown TABLE SII to find SLME are provided in the supporting information. The FIG. 3 shows that SLME using both PBE and TB-mBJ at 300 K temperature increases with the increase of the thickness. The estimated SLME at a temperature of 300 K and thickness of 500 nm using PBE and TB-mBJ potential are 13.8%, 14.0%, 11.1% and 3.9%, 4.1%, 1.96% for the increasing Br concentrations of 0.25, 0.50 and 0.75, respectively. The equal admixture of I and Br in $\text{RbPb}(\text{I}_{1-x}\text{Br}_x)_3$ shows the highest efficiency (SLME) when it is estimated with both PBE and TB-mBJ. The higher bandgaps estimated using TB-mBJ is responsible for such low SLME.

IV. CONCLUSION

In summary, the first principle calculations using PBE and TB-mBJ potential have been carried out to investigate the effect of iodide-bromide mixing in RbPbI_3 on the electronic and optical properties. The calculated bandstructures show all $\text{RbPb}(\text{I}_{1-x}\text{Br}_x)_3$ structures have indirect bandgaps. The lowest bandgap of 2.288 and 2.986 eV are estimated for $x = 0.50$ using PBE and TB-mBJ, respectively. PDOS analysis exhibits the ascending contribution of Br-4p in the conduction band region with the increasing Br concentration. The calculated TDOS depicts a large number of available states for both $\text{RbPb}(\text{I}_{0.75}\text{Br}_{0.25})_3$ and $\text{RbPb}(\text{I}_{0.25}\text{Br}_{0.75})_3$, therefore, this enhances the probability of high charge carrier concentrations. The absorption estimated using TB-mBJ also shifts to the higher energy region than that using PBE. The absorption also decreases with increasing Br concentration. The effective masses using both PBE and TB-mBJ for all the structures are found to be low and, thus, is beneficial for the ease of the carrier transport. In case of TB-mBJ potential, the binding energy of exciton is high for $x = 0.75$ whereas it is low for all other cases. The highest SLME of 14.0% using PBE and 4.1% using TB-mBJ are observed for $\text{RbPb}(\text{I}_{0.50}\text{Br}_{0.50})_3$. $\text{RbPb}(\text{I}_{0.50}\text{Br}_{0.50})_3$ shows the lowest bandgap and also highest efficiency than all other structures under our investigation, hence, turns out to be the suitable one for the photovoltaic operation.

-
- [1] P. Gao, M. Grätzel, and M. K. Nazeeruddin, Organohalide lead perovskites for photovoltaic applications, *Energy & Environmental Science* **7**, 2448 (2014).
 [2] M. A. Green, A. Ho-Baillie, and H. J. Snaith, The emergence of perovskite solar cells, *Nature photonics* **8**, 506 (2014).
 [3] A. Balilonda, Q. Li, M. Tebyetekerwa, R. Tusiime, H. Zhang, R. Jose, F. Zabihi, S. Yang, S. Ramakrishna, and M. Zhu, Perovskite solar fibers: current status, issues and challenges, *Advanced Fiber Materials* **1**, 101 (2019).

- [4] F. Zabihi, M. Tebyetekerwa, Z. Xu, A. Ali, A. K. Kumi, H. Zhang, R. Jose, S. Ramakrishna, and S. Yang, Perovskite solar cell-hybrid devices: thermoelectrically, electrochemically, and piezoelectrically connected power packs, *Journal of Materials Chemistry A* **7**, 26661 (2019).
- [5] W.-J. Yin, T. Shi, and Y. Yan, Unique properties of halide perovskites as possible origins of the superior solar cell performance, *Advanced Materials* **26**, 4653 (2014).
- [6] W. S. Yang, B.-W. Park, E. H. Jung, N. J. Jeon, Y. C. Kim, D. U. Lee, S. S. Shin, J. Seo, E. K. Kim, J. H. Noh, *et al.*, Iodide management in formamidinium-lead-halide-based perovskite layers for efficient solar cells, *Science* **356**, 1376 (2017).
- [7] J. Feng and B. Xiao, Crystal structures, optical properties, and effective mass tensors of $\text{ch}_3\text{nh}_3\text{pbx}_3$ ($x = \text{i}$ and br) phases predicted from hse06, *The Journal of Physical Chemistry Letters* **5**, 1278 (2014).
- [8] G. Giorgi, J.-I. Fujisawa, H. Segawa, and K. Yamashita, Small photocarrier effective masses featuring ambipolar transport in methylammonium lead iodide perovskite: a density functional analysis, *The journal of physical chemistry letters* **4**, 4213 (2013).
- [9] M. H. Du, Efficient carrier transport in halide perovskites: theoretical perspectives, *Journal of Materials Chemistry A* **2**, 9091 (2014).
- [10] I. M. De Los Santos, H. J. Cortina-Marrero, M. Ruíz-Sánchez, L. Hechavarría-Difur, F. Sánchez-Rodríguez, M. Courel, and H. Hu, Optimization of $\text{ch}_3\text{nh}_3\text{pb}_3\text{i}_3$ perovskite solar cells: A theoretical and experimental study, *Solar Energy* **199**, 198 (2020).
- [11] B. Farhadi, F. Zabihi, Y. Zhou, and A. Liu, A theoretical survey on the potential performance of a perovskite solar cell based on an ultrathin organic-inorganic electron transporting layer, (2021).
- [12] W.-J. Yin, T. Shi, and Y. Yan, Unique properties of halide perovskites as possible origins of the superior solar cell performance, *Advanced Materials* **26**, 4653 (2014).
- [13] W.-J. Yin, T. Shi, and Y. Yan, Unusual defect physics in $\text{ch}_3\text{nh}_3\text{pb}_3\text{i}_3$ perovskite solar cell absorber, *Applied Physics Letters* **104**, 063903 (2014).
- [14] J. Kim, S.-H. Lee, J. H. Lee, and K.-H. Hong, The role of intrinsic defects in methylammonium lead iodide perovskite, *The journal of physical chemistry letters* **5**, 1312 (2014).
- [15] W. Nie, H. Tsai, R. Asadpour, J.-C. Blancon, A. J. Neukirch, G. Gupta, J. J. Crochet, M. Chhowalla, S. Tretiak, M. A. Alam, *et al.*, High-efficiency solution-processed perovskite solar cells with millimeter-scale grains, *Science* **347**, 522 (2015).
- [16] Q. Dong, Y. Fang, Y. Shao, P. Mulligan, J. Qiu, L. Cao, and J. Huang, Electron-hole diffusion lengths $> 175 \mu\text{m}$ in solution-grown $\text{ch}_3\text{nh}_3\text{pb}_3\text{i}_3$ single crystals, *Science* **347**, 967 (2015).
- [17] Y. Yang and J. You, Make perovskite solar cells stable, *Nature* **544**, 155 (2017).
- [18] K. Brinkmann, J. Zhao, N. Pourdavoud, T. Becker, T. Hu, S. Olthof, K. Meerholz, L. Hoffmann, T. Gahlmann, R. Heiderhoff, *et al.*, Suppressed decomposition of organometal halide perovskites by impermeable electron-extraction layers in inverted solar cells, *Nature communications* **8**, 1 (2017).
- [19] Y. Zhao, J. Wei, H. Li, Y. Yan, W. Zhou, D. Yu, and Q. Zhao, A polymer scaffold for self-healing perovskite solar cells, *Nature communications* **7**, 1 (2016).
- [20] Q. Tai, P. You, H. Sang, Z. Liu, C. Hu, H. L. Chan, and F. Yan, Efficient and stable perovskite solar cells prepared in ambient air irrespective of the humidity, *Nature communications* **7**, 1 (2016).
- [21] Z. Li, M. Yang, J.-S. Park, S.-H. Wei, J. J. Berry, and K. Zhu, Stabilizing perovskite structures by tuning tolerance factor: formation of formamidinium and cesium lead iodide solid-state alloys, *Chemistry of Materials* **28**, 284 (2016).
- [22] B. Li, L. Fu, S. Li, H. Li, L. Pan, L. Wang, B. Chang, and L. Yin, Pathways toward high-performance inorganic perovskite solar cells: challenges and strategies, *Journal of Materials Chemistry A* **7**, 20494 (2019).
- [23] T. Liu, Y. Zong, Y. Zhou, M. Yang, Z. Li, O. S. Game, K. Zhu, R. Zhu, Q. Gong, and N. P. Padture, High-performance formamidinium-based perovskite solar cells via microstructure-mediated δ -to- α phase transformation, *Chemistry of Materials* **29**, 3246 (2017).
- [24] X. Zhang, X. Ren, B. Liu, R. Munir, X. Zhu, D. Yang, J. Li, Y. Liu, D.-M. Smilgies, R. Li, *et al.*, Stable high efficiency two-dimensional perovskite solar cells via cesium doping, *Energy & Environmental Science* **10**, 2095 (2017).
- [25] M. Kulbak, S. Gupta, N. Kedem, I. Levine, T. Bendikov, G. Hodes, and D. Cahen, Cesium enhances long-term stability of lead bromide perovskite-based solar cells, *The journal of physical chemistry letters* **7**, 167 (2016).
- [26] R. J. Sutton, G. E. Eperon, L. Miranda, E. S. Parrott, B. A. Kamino, J. B. Patel, M. T. Hörlantner, M. B. Johnston, A. A. Haghighirad, D. T. Moore, *et al.*, Bandgap-tunable cesium lead halide perovskites with high thermal stability for efficient solar cells, *Advanced Energy Materials* **6**, 1502458 (2016).
- [27] C.-Y. Chen, H.-Y. Lin, K.-M. Chiang, W.-L. Tsai, Y.-C. Huang, C.-S. Tsao, and H.-W. Lin, All-vacuum-deposited stoichiometrically balanced inorganic cesium lead halide perovskite solar cells with stabilized efficiency exceeding 11%, *Advanced materials* **29**, 1605290 (2017).
- [28] A. Swarnkar, A. R. Marshall, E. M. Sanehira, B. D. Chernomordik, D. T. Moore, J. A. Christians, T. Chakrabarti, and J. M. Luther, Quantum dot-induced phase stabilization of α - $\text{cs}_2\text{pb}_3\text{i}_3$ perovskite for high-efficiency photovoltaics, *Science* **354**, 92 (2016).
- [29] M. M. Lee, J. Teuscher, T. Miyasaka, T. N. Murakami, and H. J. Snaith, Efficient hybrid solar cells based on meso-structured organometal halide perovskites, *Science* **338**, 643 (2012).
- [30] J. H. Noh, S. H. Im, J. H. Heo, T. N. Mandal, and S. I. Seok, Chemical management for colorful, efficient, and stable inorganic-organic hybrid nanostructured solar cells, *Nano letters* **13**, 1764 (2013).
- [31] S. Colella, E. Mosconi, P. Fedeli, A. Listorti, F. Gazza, F. Orlandi, P. Ferro, T. Besagni, A. Rizzo, G. Calestani, *et al.*, $\text{Mapb}_3\text{i}_3\text{-xcl}_x$ mixed halide perovskite for hybrid solar cells: the role of chloride as dopant on the transport and structural properties, *Chemistry of Materials* **25**, 4613 (2013).

- [32] B. Suarez, V. Gonzalez-Pedro, T. S. Ripolles, R. S. Sanchez, L. Otero, and I. Mora-Sero, Recombination study of combined halides (cl, br, i) perovskite solar cells, *The journal of physical chemistry letters* **5**, 1628 (2014).
- [33] E. Edri, S. Kirmayer, A. Henning, S. Mukhopadhyay, K. Gartsman, Y. Rosenwaks, G. Hodes, and D. Cahen, Why lead methylammonium tri-iodide perovskite-based solar cells require a mesoporous electron transporting scaffold (but not necessarily a hole conductor), *Nano letters* **14**, 1000 (2014).
- [34] B. Suarez, V. Gonzalez-Pedro, T. S. Ripolles, R. S. Sanchez, L. Otero, and I. Mora-Sero, Recombination study of combined halides (cl, br, i) perovskite solar cells, *The journal of physical chemistry letters* **5**, 1628 (2014).
- [35] E. Edri, S. Kirmayer, M. Kulbak, G. Hodes, and D. Cahen, Chloride inclusion and hole transport material doping to improve methyl ammonium lead bromide perovskite-based high open-circuit voltage solar cells, *The Journal of Physical Chemistry Letters* **5**, 429 (2014).
- [36] J. H. Noh, S. H. Im, J. H. Heo, T. N. Mandal, and S. I. Seok, Chemical management for colorful, efficient, and stable inorganic–organic hybrid nanostructured solar cells, *Nano letters* **13**, 1764 (2013).
- [37] A. Nyayban, S. Panda, A. Chowdhury, and B. I. Sharma, First principle studies of rubidium lead halides towards photovoltaic application, *Materials Today Communications* **24**, 101190 (2020).
- [38] P. Blaha, K. Schwarz, G. K. Madsen, D. Kvasnicka, J. Luitz, *et al.*, wien2k, An augmented plane wave+ local orbitals program for calculating crystal properties (2001).
- [39] J. P. Perdew, K. Burke, and M. Ernzerhof, Generalized gradient approximation made simple, *Physical review letters* **77**, 3865 (1996).
- [40] P.-P. Sun, Q.-S. Li, S. Feng, and Z.-S. Li, Mixed Ge/Pb perovskite light absorbers with an ascendant efficiency explored from theoretical view, *Physical Chemistry Chemical Physics* **18**, 14408 (2016).
- [41] J. Qian, B. Xu, and W. Tian, A comprehensive theoretical study of halide perovskites ABX₃, *Organic Electronics* **37**, 61 (2016).
- [42] M. Pazoki, T. J. Jacobsson, A. Hagfeldt, G. Boschloo, and T. Edvinsson, Effect of metal cation replacement on the electronic structure of metalorganic halide perovskites: Replacement of lead with alkaline-earth metals, *Physical Review B* **93**, 144105 (2016).
- [43] M. Shirayama, H. Kadowaki, T. Miyadera, T. Sugita, M. Tamakoshi, M. Kato, T. Fujiseki, D. Murata, S. Hara, T. N. Murakami, *et al.*, Optical transitions in hybrid perovskite solar cells: ellipsometry, density functional theory, and quantum efficiency analyses for CH₃NH₃PbI₃, *Physical Review Applied* **5**, 014012 (2016).
- [44] A. Nyayban, S. Panda, and A. Chowdhury, Structural, electronic and optical properties of lead free rb based triiodide for photovoltaic application: an ab initio study, *Journal of Physics: Condensed Matter* **33**, 375702 (2021).
- [45] P.-P. Sun, Q.-S. Li, S. Feng, and Z.-S. Li, Mixed Ge/Pb perovskite light absorbers with an ascendant efficiency explored from theoretical view, *Physical Chemistry Chemical Physics* **18**, 14408 (2016).
- [46] F. Tran and P. Blaha, Accurate band gaps of semiconductors and insulators with a semilocal exchange-correlation potential, *Physical review letters* **102**, 226401 (2009).
- [47] H. Dixit, N. Tandon, S. Cottenier, R. Saniz, D. Lamoen, B. Partoens, V. Van Speybroeck, and M. Waroquier, Electronic structure and band gap of zinc spinel oxides beyond lda: ZnAl₂O₄, ZnGa₂O₄ and ZnIn₂O₄, *New Journal of Physics* **13**, 063002 (2011).
- [48] B. Traoré, G. Boudier, W. Lafargue-Dit-Hauret, X. Rocquefelte, C. Katan, F. Tran, and M. Kepenekian, Efficient and accurate calculation of band gaps of halide perovskites with the tran-blaha modified becke-johnson potential, *Physical Review B* **99**, 035139 (2019).
- [49] F. D. Murnaghan, Finite deformations of an elastic solid, *American Journal of Mathematics* **59**, 235 (1937).
- [50] H. M. Ghaithan, Z. A. Alahmed, S. M. Qaid, and A. S. Aldwayyan, Density functional theory analysis of structural, electronic, and optical properties of mixed-halide orthorhombic inorganic perovskites, *ACS omega* **6**, 30752 (2021).
- [51] R. Mayengbam, S. Tripathy, and G. Palai, First-principle insights of electronic and optical properties of cubic organic–inorganic mnxpb(1-x)i3 perovskites for photovoltaic applications, *The Journal of Physical Chemistry C* **122**, 28245 (2018).